CrossMark

Rapid Optical Flares in the Blazar OJ 287 on Intraday Timescales with TESS

Shubham Kishore[1,2] , Alok C. Gupta[1,3] , and Paul J. Wiita[4]
[1] Aryabhatta Research Institute of Observational Sciences (ARIES), Manora Peak, Nainital 263001, India; amp700151@gmail.com, acgupta30@gmail.com
[2] Department of Physics, DDU Gorakhpur University, Gorakhpur 273009, India
[3] Key Laboratory for Research in Galaxies and Cosmology, Shanghai Astronomical Observatory, Chinese Academy of Sciences, Shanghai 200030, People's Republic of China
[4] Department of Physics, The College of New Jersey, 2000 Pennington Rd., Ewing, NJ 08628-0718, USA; wiitap@tcnj.edu

Abstract

We have analyzed the optical light curves of the blazar OJ 287 obtained with the Transiting Exoplanet Survey Satellite over about 80 days from 2021 October 13 to December 31, with an unprecedented sampling of 2 minutes. Although significant variability has been found during the entire period, we have detected two exceptional flares with flux nearly doubling and then nearly tripling over 2 days in the middle of 2021 November. We went through the light-curve analysis using the excess variance, generalized Lomb–Scargle periodogram, and continuous autoregressive moving average methods and estimated the flux halving/doubling timescales. The most probable shortest variability timescale was found to be 0.38 days in the rising phase of the first flare. We briefly discuss some emission models for the variability in radio-loud active galactic nuclei that could be capable of producing such fast flares.

Unified Astronomy Thesaurus concepts: Blazars (164); Active galactic nuclei (16); BL Lacertae objects (158); Jets (870)

1. Introduction

The blazar subclass of radio-loud (RL) active galactic nuclei (AGN) displays flux, spectral, and polarization variability throughout the electromagnetic (EM) spectrum on diverse timescales ranging from a few minutes to several years. Blazar emission is predominantly nonthermal. Probably the least well understood temporal variability is observed on timescales of minutes to several hours and is commonly called microvariability (Miller et al. 1989) or intraday variability (IDV; Wagner & Witzel 1995). Microvariability in optical flux provides a strong route toward understanding the physical processes occurring in the most compact emitting regions of blazars.

Miller et al. (1989) made the pioneering discovery of optical microvariability in the blazar BL Lacerate, and in the subsequent ∼3.5 decades, many of the brighter blazars have been observed for the study of microvariability during thousands of observing nights using various telescopes (e.g., Miller et al. 1989; Carini et al. 1992; Wagner et al. 1993; Heidt & Wagner 1996; Sagar et al. 1999; Qian et al. 2002; Sagar et al. 2004; Montagni et al. 2006; Gupta et al. 2008; Poon et al. 2009; Gaur et al. 2012; Agarwal & Gupta 2015; Goyal et al. 2018; Wehrle et al. 2019; Pandey et al. 2020; Kalita et al. 2021; Raiteri et al. 2021; Dhiman et al. 2023; Pininti et al. 2023; Wehrle et al. 2023, and references therein). In a statistical study of optical microvariability properties of various classes of AGN, Gupta & Joshi (2005) found that if a blazar is observed continuously for less than 6 hr, the chance of seeing microvariations is ≈60%–65%, but it rises to 80%–85% for nightly observations that exceed 6 hr.

OJ 287, at redshift $z = 0.306$ (Sitko & Junkkarinen 1985), is among the few AGN that probably host a supermassive black hole (SMBH) binary system. OJ 287 has been observed in optical bands since 1888, and by using this century-long data, Sillanpaa et al. (1988) discovered that the blazar shows outbursts with a period of ∼12 yr and proposed a binary SMBH model to explain it. Because of this short orbital period, OJ 287 is thus a candidate to emit nanohertz (nHz) gravitational waves (GWs) (e.g., Valtonen et al. 2021, 2023, and references therein). OJ 287 has been studied extensively for optical variabilities on diverse timescales, e.g., microvariability, short-term variability, and long-term variability (e.g., Sillanpaa et al. 1996a, 1996b; Gupta et al. 2017; Goyal et al. 2018; Gupta et al. 2019; Wehrle et al. 2019, 2023, and references therein).

Here we consider data taken on OJ 287 over a span of about 80 days (from 2021 October 13 to 2021 December 31) by the Transiting Exoplanet Survey Satellite (TESS).[5] Our focus is on a continuous and uniformly sampled set of observations, more precisely the first segment of Sector 45 that spans ∼12 days with a time resolution of 2 minutes. These data provide us an excellent opportunity to study optical microvariability of a blazar with essentially uniform sampling made at the shortest time resolution and over a quite extended duration. We found a double-peaked strong flare in the light curve (LC) that spanned about 2 days. We are unaware of a previous clear case for such a well-resolved double-peaked flare on such timescales. OJ 287 was earlier observed from the Kepler satellite in its K2 mission phase for a continuous period of 75 days (2015 April 27–2015 July 10) and this uniformly sampled optical LC displayed several significant flares (Goyal et al. 2018; Wehrle et al. 2019), but none as fast with as large an amplitude as those we see in these TESS data. Wehrle et al. (2023) analyzed a subsequent K2 observation of the source taken for 51 days (from 2018 May 13 to 2018 July 2) and also reported multiple rapid, but not quite as strong, flares during this epoch.

[5] http://tess.gsfc.nasa.gov
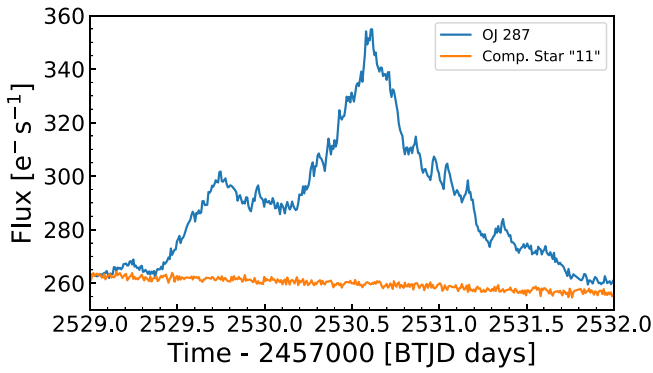
Figure 1. Partial Sector 45 LCs of OJ 287 and comparison star 11 during the strongest flares.

In Section 2, we describe data acquisition and reduction. In Section 3, we explain the data analysis techniques we used and present results. A discussion is provided in Section 4.

2. Data Acquisition and Reduction

Aside from some data gaps of 1–2 days related to telemetry, OJ 287 was observed essentially continuously by TESS; its detector bandpass spans the range 600–1000 nm and is centered at the traditional Cousins *I* band.[6] These observations spanned ∼80 days across Sectors 44, 45, and 46, with a cadence of 2 minutes; the specific data we used are available from the Mikulski Archive for Space Telescopes (MAST) at doi:10.17909/b3et-af14. We have used the PDCSAP_FLUX (Jenkins et al. 2016) values for reduction as described in Kishore et al. (2023) and have followed the reduction procedure given there. Hence, we refer the readers to that paper for the nomenclature used in this section and the optimum values found for the three parameters employed during data reduction: the two goodness metrics (overfitting and underfitting) and the regularization factor (α).

Unfortunately there were no LC files for nearby comparison stars (which contain SAP and PDCSAP fluxes) from the TESS pipeline already available, because these values are made available only for preselected targets. TESS also created full-frame images (FFIs) of the portions of sky observed at a cadence of 20 minutes for those sectors, so we used these FFIs to extract the SAP LCs of comparison stars 4, 10, and 11 (Smith et al. 1985) along with that of OJ 287 to confirm that our source's variability is intrinsic. Comparison stars 4 and 10 had substantially higher fluxes than OJ 287, so in Figure 1 we used star 11, with a very comparable brightness, to illustrate the genuine variability of the source.

It should be emphasized that Figure 1 provides a preliminary version of the LC that provides a useful visual comparison, but a more fully reduced version has been used in our actual analysis of the LC of OJ 287.

Table 1 includes the values of these fitting parameters obtained for reduction of PDCSAP_FLUX of our object for each of the sectors. As discussed in Kishore et al. (2023), the values of both the underfitting and overfitting goodness metrics should be kept at or above 0.8, consistent with the lowest possible α value. For Sector 45, the overfitting metric was below 0.8 at $\alpha = 0.1$, so the optimum value of α was found to be 0.34 when the overfitting metric crosses the critical limit of
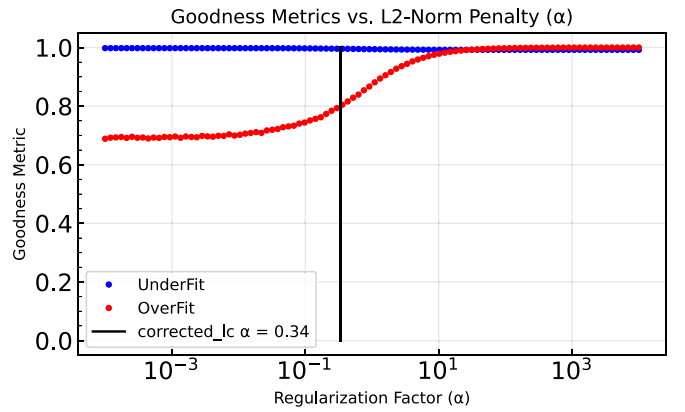
Figure 2. Goodness metric scan plot for the TESS Sector 45 observation of OJ 287.

Table 1
Flux Calibration Details

| Sector	α	Overfitting Metric	Underfitting Metric
44	0.10	0.968	0.999
45	0.34	0.801	0.996
46	0.10	0.984	1.000

0.8. Figure 2 illustrates these conditions for the Sector 45 LC reduction. Figure 3 includes two plots for each of the sectors. The upper panel in each set contains the raw LC and the different co-trending basis vectors used for the reduction, while the lower panel compares the raw LC and reduced LC. Variability is seen in all three of these LCs, but it is much stronger in Sector 45. In Figure 4 we show the zoomed-in Sector 45 reduced LC, showing the double flare in the first segment of this sector in more detail.

3. Data Analysis and Results

3.1. Excess Variance and Flares

Flux variability is one of the fundamental properties of a typical blazar across all EM bands; however, an additional variance is present in all LCs from the measurement errors in the observations. The excess variance method incorporates the measurement errors as well in quantifying the variability. The fractional rms variability amplitude, which is the square root of normalized excess variance, and corresponding uncertainty, have been computed as in Vaughan et al. (2003). In our analysis of $F_{\rm var}$ for the two flares in the first segment of Sector 45, the average flux counts after removing the two flares from the segment (where the determination of the start and end of the flares was done visually, selecting the minima in the LC nearest to the flaring span) was used as the baseline flux. This value came out to be ∼193 e$^-$ s^{-1}. The maximum flux values during the two flares are ∼349 e$^-$ s^{-1} and ∼566 e$^-$ s^{-1}, respectively, corresponding to nominal increases of ∼81% and ∼194%, respectively. With this baseline, the LC shows an overall $F_{\rm var}$ of 72% during the total flaring period. Table 2 includes the $F_{\rm var}$ obtained for the two flares along with the other parameters describing the flares.
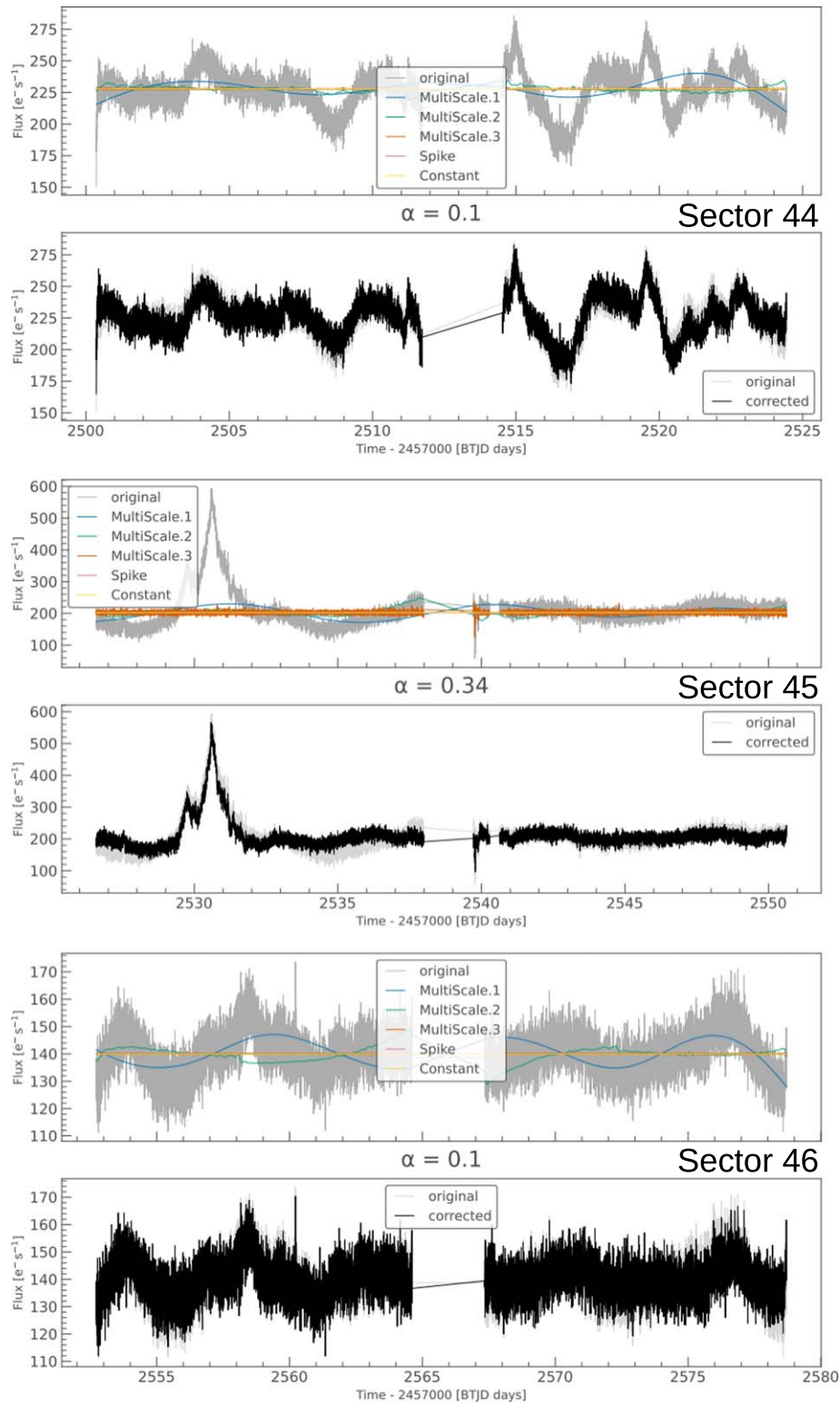
Figure 3. Raw and reduced LCs of OJ 287 observed in all three sectors. The upper panels include the original PDCSAP fluxes and the co-trending basis vectors that are used to correct it, and the bottom panels show the original and corrected LCs corresponding to each labeled sector.

3.2. Variability Timescales

We have used the halving/doubling timescale given as

$$F(t) = F(t_0)2^{(t-t_0)/\tau} \quad (t > t_0), \qquad (1)$$

where τ and $F(t)$ are the characteristic halving/doubling timescale and the flux value at time t. In our analysis, we

first divided each flare into two parts: a "rising phase" and a "declining phase" and then examined each and every possible distinct pair of data points within each flare. We then imposed a selection criterion so that only those data point pairs, where the differences in flux were greater than 3σ, were considered for the estimation of τ (Foschini et al. [2011]). The doubling/

3
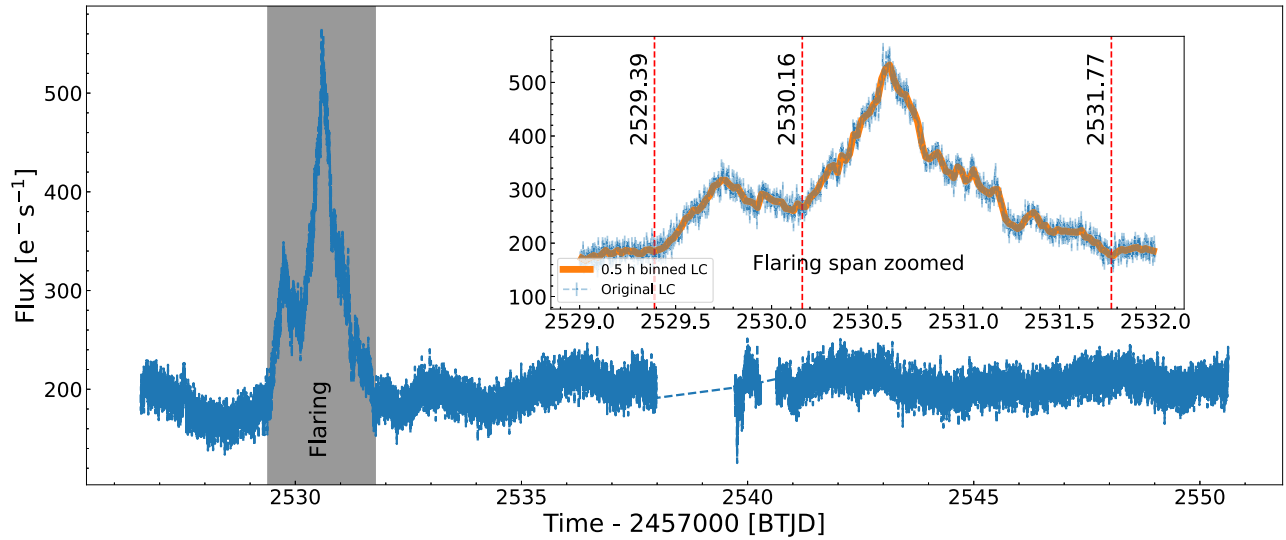
Figure 4. The main plot includes the complete reduced Sector 45 LC. The subplot zooms in on the flare period; for better visualization of the trend, a 0.5 hr binned LC has been overplotted.

Table 2
Flare Characteristics

Flare	Flare Peak Epoch (BTJD)	Flare Peak Flux ($e^- s^{-1}$)	Difference of Flare Peak and Baseline ($e^- s^{-1}$)	F_{var} (%)	τ (days) (Rising Phase)	τ (days) (Declining Phase)	Spectral Index (α)	KS Test p-value
1	2529.74	349	156	42.9	0.38 ± 0.10	-0.41 ± 0.21	-1.89 ± 0.12	0.91
2	2530.58	566	373	82.4	0.44 ± 0.09	-0.79 ± 0.25	-2.20 ± 0.13	0.98

halving time was estimated for each obtained pair. Thus, for each of the two phases of the two flares, the obtained ensemble of distinct pairs led to a distribution of the timescale. Figure 5 shows the distribution of the τ estimates obtained for the two pairs of rising and declining phases, and Table 2 includes the most probable timescales with the corresponding uncertainties (after fitting the distribution with a Gaussian function) for each of the four flaring phases, as well as the times of the two peaks. It should be noted that there is a tiny positive fluctuation during the declining phase of the LC during the first flare between epochs 2529.921 to 2529.953; so we dropped this small rising fluctuation from the declining phase while evaluating τ. The two portions of the declining phase, from 2529.740 to 2529.921 and from 2529.953 to 2530.160, led to separate sets of τ values. These two sets of τ values were combined to give the composite timescale distribution of this declining phase, shown in the upper right panel of Figure 5.

3.3. Periodograms

Apart from the variability timescales that may be associated with the size of the emitting region, the spectral index of the periodogram, or the power spectral density (PSD) slope, can yield information about the source of the variability. Various physical models naturally yield somewhat different ranges of spectral indices (e.g., Pollack et al. 2016; Wehrle et al. 2019). We have used the generalized Lomb–Scargle periodogram as in Kishore et al. (2023) for the analysis of all six segments of the three sectors, as well as the first flare and the second flare of Sector 45 individually. As usual, the PSDs so obtained flatten to instrumental white noise in the high-frequency regime, so we used cutoff frequencies (Gierliński et al. 2008; Lachowicz et al.

2009) for each segment, which varied somewhat, while conservatively fitting the PSDs in the red-noise region with power laws ($P(\nu) = A\nu^{\alpha}$). To test the power-law fit to the PSD, we followed the approach of Vaughan (2005). This involved considering twice the ratio of the periodogram to the fitting model at each frequency. The set of these ratios was used to form a cumulative distribution function (CDF). Ideally this CDF should follow that of a χ_2^2 (χ^2 distribution with 2 degrees of freedom; Vaughan 2005). Under the null hypothesis that these two distributions are the same, Kolmogorov–Smirnov (KS) tests were performed for each PSD fitting. The p-values (probability of not discarding the null hypothesis) were evaluated for each comparison of segment-wise fits, and the high p-values we obtained (given in Table 3) do indicate good PSD fits. The scipy[7] python package was used for the goodness-of-fit estimation, following the steps described in Vaughan (2005). An oversampling by a factor of 5 has been employed in the Lomb–Scargle periodogram calculation as there is a paucity of data points in the low-frequency red-noise region.

Figure 6 displays the PSD behaviors of the first segment of the Sector 45 LC, and Table 3 gives the spectral indices we obtained for all six of the segments. The PSD slopes have typically high values (close to or greater than 2) up through the segment including the flares, but following that, there seems to be a considerable flattening of the PSD slopes in the later segments. The overall PSD slopes during the flares and during the entire segment of Sector 45 agree within the errors.

The PSD slope values listed in Table 3 for several segments cover quite a wide range. Hence, they unfortunately cannot be used to eliminate any of the rather small number of models for

---

[7] https://scipy.org/
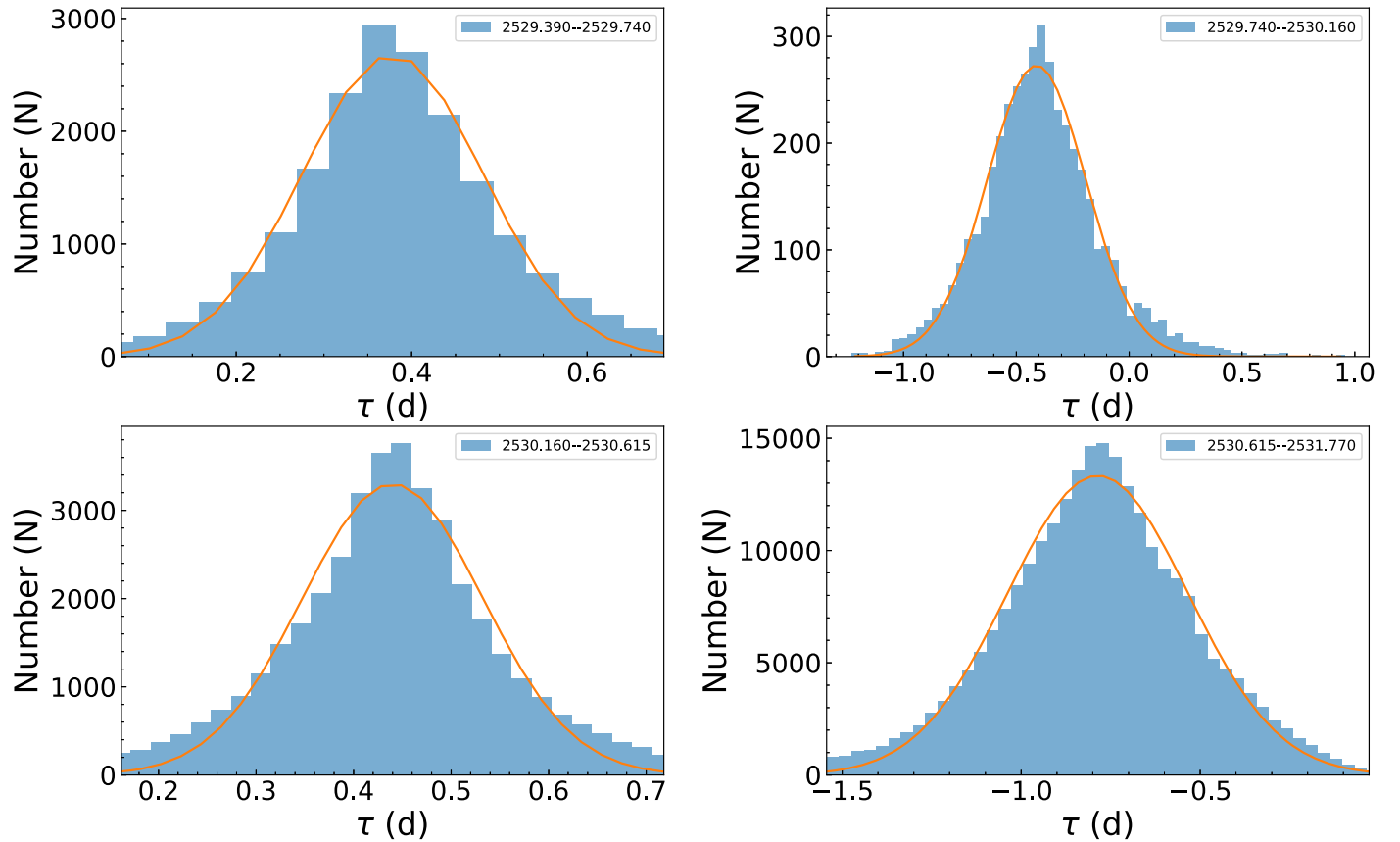
Figure 5. Each panel shows the distribution of doubling/halving timescales corresponding to the labeled time spans. Positive values of τ indicate the rising phases and negative ones the declining phases of the flares. The orange curve in each panel shows the Gaussian fit determining the best value of τ.

Table 3
Segment-wise PSD and CARMA Results

Sector/ Segment	Cutoff Freqs. (d^{-1})	Spectral Index (α)	KS Test p-value	CARMA (p, q)
44/1	$0.25-7.00$	-1.99 ± 0.09	0.93	(1,0)
44/2	$0.15-7.00$	-2.56 ± 0.09	0.99	(1,0)
45/1	$0.07-20.0$	-2.14 ± 0.04	0.95	(1,0)
45/2	$0.08-10.0$	-1.41 ± 0.06	1.00	(1,0)
46/1	$0.04-7.00$	-1.56 ± 0.07	0.95	(2,1)
46/2	$0.08-10.0$	-1.05 ± 0.06	1.00	(2,0)

blazar variability that have evaluated the resulting PSDs (e.g., Pollack et al. 2016; Wehrle et al. 2019; Kadowaki et al. 2021), each of which is, or appears to be, capable of yielding a span of slopes within this range.

3.4. CARMA Modeling

Although the great majority of the analyses of AGN LCs in the literature have focused on periodogram slopes, a more sophisticated approach to analyzing the structure of LCs involves considering autoregressive (AR), moving average (MA), models, which in their continuous version are given the acronym CARMA (e.g., Kelly et al. 2009, 2014; Kasliwal et al. 2017; Goyal et al. 2018). CARMA models employ the plausible assumption that an LC is a realization of a Gaussian noise process. Specifically, a CARMA(p, q) model connects the LC and its first p time derivatives to the noise and its first q time derivatives (for the definitions used here, see Kelly et al.

2014, Equation (1), and accompanying text). A CARMA(1,0) model is equivalent to a damped random walk, or an Ornstein–Ulenbeck process, and seems to better describe the long-term LCs of many quasars than does a single periodogram slope (e.g., Kelly et al. 2009, 2014).

A physical interpretation of this approach is that the AR part of the model describes the short-term memory in the system, while the MA part indicates how the amplitudes of random perturbations behave on different timescales. Hence, both the correlation structure and degree of smoothness of noisy processes can be described by CARMA models (e.g., Moreno et al. 2019). Ryan et al. (2019) found that blazar γ-ray LCs were usually better fit by the modestly more complex CARMA (2,1) models than by CARMA(1,0) ones, though the number of objects for which this analysis could be done was modest. In a paper describing a very wide range of approaches to analyzing Fermi-LAT γ-ray LCs of 11 blazars, Tarnopolski et al. (2020) performed CARMA modeling of LCs binned into 7 day, 10 day, and 14 day intervals. Their results are basically consistent with those of Ryan et al. (2019); though both CARMA(1,0) and (2,1) models were most frequently optimal, occasionally (3,0) or (3,1) models were preferred.

We have performed CARMA analyses of these TESS LCs following the approach of Yu & Richards (2022),[8] which provides a fast way to produce CARMA models. All (p,q) pairs with $1 \leqslant p \leqslant 5$ and $q < p$ were considered for each of the six segments of the three sectors. After randomly generating the initial parameter values for each of the CARMA(p, q) models,

---

[8] https://github.com/ywx649999311/EzTao.git
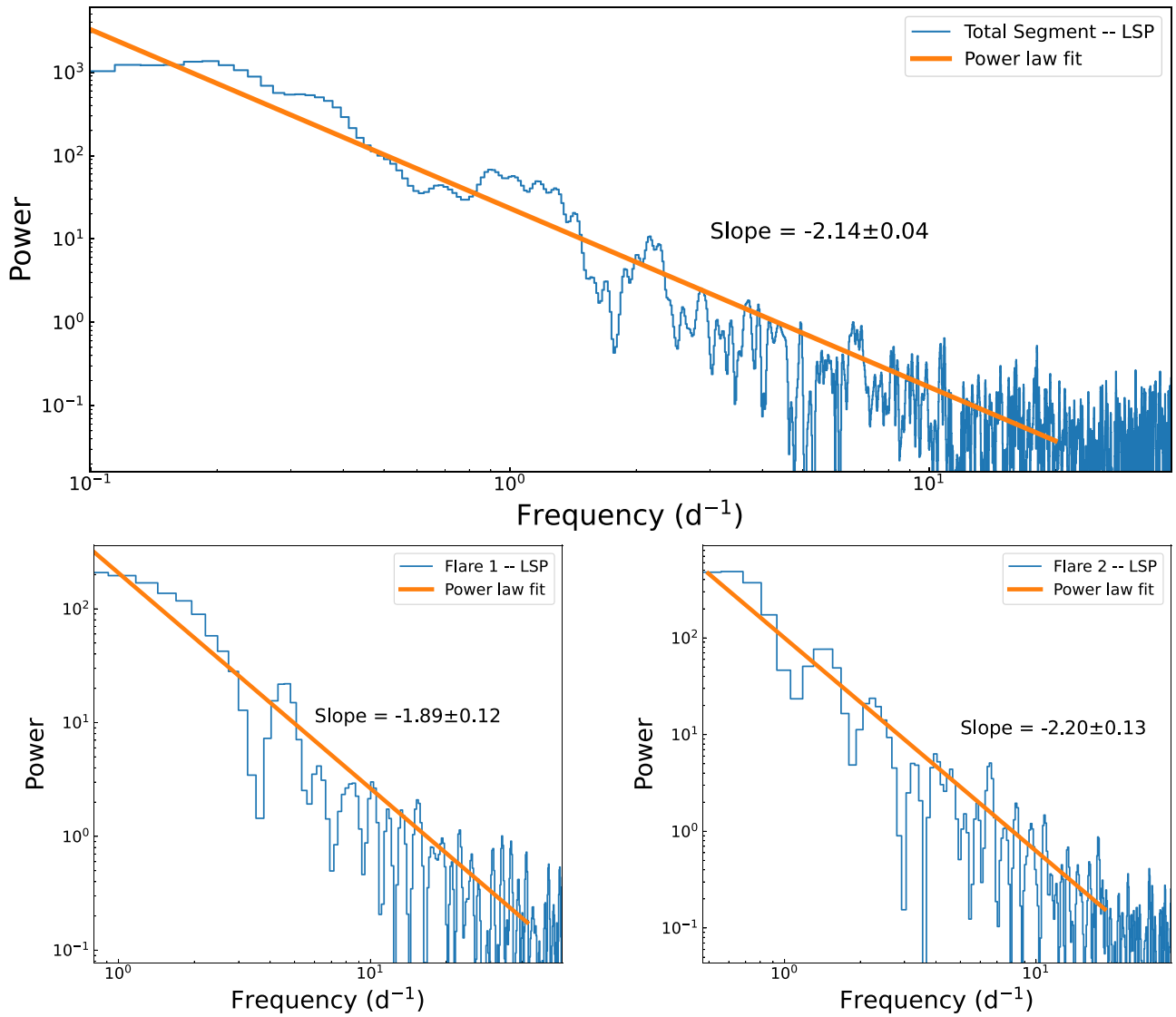
Figure 6. The panels show the Lomb–Scargle periodograms corresponding to the labeled pieces of the first segment of the Sector 45 LC with their PSD slopes.

the LCs were fitted by those models. The goodness of each fit was estimated by finding the log-likelihood value with respect to the initial LC, and the best fit was taken to be the one that maximized that quantity. The resulting best-fitting (p, q) values are given in the last column of Table 3. We see that both Sectors 44 and 45 can be characterized by a CARMA(1,0) or a damped random walk model, though the last sector, Sector 46, prefers models with $p = 2$.

4. Discussion

By comparing all the TESS observations of OJ 287 from Figure 3, it is clear that the double-peaked flare in Sector 45 illustrates a strong outburst not otherwise seen during these three sectors. From the subplot in Figure 2, it is evident that the blazar flux rises during the flares almost monotonically, but the decays involve some jerks. We also notice that the rises are faster than the decays during each of the two flare phases. Chiaberge & Ghisellini (1999) showed that symmetric LCs, with similar rise and decay timescales (Abdo et al. 2010), are expected when the cooling time of electrons $t_{cooling}$ is significantly shorter than the light-crossing time, R/c, with R

the size of the emission region. In this analysis it was assumed that the relativistic electrons are accelerated so that their energies obtain a power-law distribution. Asymmetric profiles, with decay times longer than rise times, result when $t_{cooling} > R/c$ because then the timescale for decline is longer than the timescale for rise of the flare (Chiaberge & Ghisellini 1999; Li et al. 2018).

OJ 287 was earlier observed by Kepler for a continuous period of 75 days (2015 April 27 to July 10). A uniformly sampled optical LC of OJ 287 from the first K2 observation detected several rapid flares, though none as significant on these short timescales as seen in Sector 45 (Goyal et al. 2018; Wehrle et al. 2019). Goyal et al. (2018) found that the PSD of the total LC at that time was well fitted by a CARMA(4,1) model,[9] so of a higher order than we find during the later TESS observations. It may be worth noting, though, that a CARMA (4,2) or (4,3) model was among the two runners-up to the best fits we found for five of the six segments. Wehrle et al. (2023) found the PSD slope during that period to be -2.28 ± 0.17 for long-cadence (30 minute bin) data, whereas the PSD slope was

_____

[9] https://github.com/brandonckelly/carma_pack

found to be somewhat steeper, -2.65 ± 0.05, for the short-cadence (1 minute bin) data. In the later K2 observation of OJ 287 that lasted 51 days (2018 May 13 to July 2), the flux variability shows a similar jagged behavior as during its 2015 observation. The PSD slopes for long-cadence (30 minute bin) data and short-cadence (1 minute bin) data were found to be -1.96 ± 0.20 and -2.26 ± 0.06, respectively (Wehrle et al. 2023), and so in the same range as the first three segments of the TESS observations discussed here.

Although the variable flux from blazars is dominated by jet emission, accretion disks can contribute in the low-flux state of flat-spectrum radio galaxies. Since OJ 287 is a BL Lac object and during this time it was in an overall intermediate brightness state (A.C. Gupta et al. 2023, in preparation) we can rule out the strong flux variation as arising from the accretion disk. Much of the optical (and other) variability in blazars can be explained by turbulence behind the shocks in a relativistic jet (e.g., Marscher 2014; Pollack et al. 2016) or in turbulence produced by magnetic reconnection (e.g., Guo et al. 2021; Kadowaki et al. 2021). These magnetic reconnection structures in jets can lead to very fast emission changes that typically produce flares with somewhat longer decay than rise times (Kadowaki et al. 2021), as we saw in OJ 287. The very rapid and substantial flares on sub-day timescales seen here could also arise from extremely compact regions with very high Doppler factors, as occurring in the mini-jet or jet-in-jet scenarios (e.g., Ghisellini & Tavecchio 2008; Giannios et al. 2009). In such models, portions of the plasma in the relativistic jets are accelerated to Lorentz factors ~ 100 through magnetocentrifugal or magnetic reconnection processes, and the resulting extreme Doppler boosting can yield fast and strong flux changes.

We obtained the shortest variability timescale ($\tau_{\min} = 0.38$ days) in the rising phase of the first flare. To estimate an upper limit for the size of the emission region, R, we apply the simple causality constraint,

$$R \leqslant \frac{c\,\tau_{\min}\,\delta}{1+z}\,,\qquad(2)$$

where δ represents the Doppler factor. Cohen et al. (2018) compiled values of δ for OJ 287 from the literature: $\delta = 18.9 \pm 6$ and 17.0 were derived from 43 GHz radio flares of OJ 287 in 1998–2000 and 2003, respectively (Jorstad et al. 2005; Hovatta et al. 2009). A more recent value of $\delta = 8.7$ was derived from millimeter-wave flares after 2007 (Jorstad et al. 2017; Liodakis et al. 2017). By using the complete range of Doppler factor values, 8.7 to 18.9 ± 6, taking $z = 0.306$ (Sitko & Junkkarinen 1985), applying the shortest variability timescale ($\tau_{\min} = 0.38$ days), and using Equation (2), we estimate the size of emission region to be in the range of 2.2×10^{15} cm–6.3×10^{15} cm.

We have reduced and analyzed the TESS LCs for OJ 287 spanning three consecutive sectors (44–46), which correspond to 2021 October 13 through December 31. Each sector had a ~ 2–3 day gap near its middle, so we analyzed the resulting six segments separately. All of them showed significant variability that can be approximately characterized as having PSD slopes in the range ~ -1.5 to ~ -2.5 and usually being well fit by CARMA(1,0) models. Such LCs are typical of AGN, but an unexpected result was the observation of two consecutive strong flares (with flux increases of $\sim 81\%$ and $\sim 194\%$) seen

during the first segment of Sector 45. Both of them had the most probable doubling rise times around 0.4 days and decay times that were nearly as fast, indicating that this optical emission arises from a very compact region in the relativistic jet.

ORCID iDs

Shubham Kishore ⬥ https://orcid.org/0000-0001-8716-9412
Alok C. Gupta ⬥ https://orcid.org/0000-0002-9331-4388
Paul J. Wiita ⬥ https://orcid.org/0000-0002-1029-3746

References

Abdo, A. A., Ackermann, M., Ajello, M., et al. 2010, ApJ, 722, 520
Agarwal, A., & Gupta, A. C. 2015, MNRAS, 450, 541
Carini, M. T., Miller, H. R., Noble, J. C., & Goodrich, B. D. 1992, AJ, 104, 15
Chiaberge, M., & Ghisellini, G. 1999, MNRAS, 306, 551
Cohen, M. H., Aller, H. D., Aller, M. F., et al. 2018, ApJ, 862, 1
Dhiman, V., Gupta, A. C., Kurtanidze, S. O., et al. 2023, MNRAS, 519, 2796
Foschini, L., Ghisellini, G., Tavecchio, F., Bonnoli, G., & Stamerra, A. 2011, A&A, 530, A77
Gaur, H., Gupta, A. C., Strigachev, A., et al. 2012, MNRAS, 425, 3002
Ghisellini, G., & Tavecchio, F. 2008, MNRAS, 386, L28
Giannios, D., Uzdensky, D. A., & Begelman, M. C. 2009, MNRAS, 395, L29
Gierliński, M., Middleton, M., Ward, M., & Done, C. 2008, Natur, 455, 369
Goyal, A., Stawarz, Ł., & Zola, S. 2018, ApJ, 863, 175
Guo, F., Li, X., Daughton, W., et al. 2021, ApJ, 919, 111
Gupta, A. C., Agarwal, A., Mishra, A., et al. 2017, MNRAS, 465, 4423
Gupta, A. C., Fan, J. H., Bai, J. M., & Wagner, S. J. 2008, AJ, 135, 1384
Gupta, A. C., Gaur, H., Wiita, P. J., et al. 2019, AJ, 157, 95
Gupta, A. C., & Joshi, U. C. 2005, A&A, 440, 855
Heidt, J., & Wagner, S. J. 1996, A&A, 305, 42
Hovatta, T., Valtaoja, E., Tornikoski, M., & Lähteenmäki, A. 2009, A&A, 494, 527
Jenkins, J. M., Twicken, J. D., McCauliff, S., et al. 2016, Proc. SPIE, 9913, 99133E
Jorstad, S. G., Marscher, A. P., Lister, M. L., et al. 2005, AJ, 130, 1418
Jorstad, S. G., Marscher, A. P., Morozova, D. A., et al. 2017, ApJ, 846, 98
Kadowaki, L. H. S., de Gouveia Dal Pino, E. M., Medina-Torrejón, T. E., Mizuno, Y., & Kushwaha, P. 2021, ApJ, 912, 109
Kalita, N., Gupta, A. C., & Gu, M. 2021, ApJS, 257, 41
Kasliwal, V. P., Vogeley, M. S., & Richards, G. T. 2017, MNRAS, 470, 3027
Kelly, B. C., Bechtold, J., & Siemiginowska, A. 2009, ApJ, 698, 895
Kelly, B. C., Becker, A. C., Sobolewska, M., Siemiginowska, A., & Uttley, P. 2014, ApJ, 788, 33
Kishore, S., Gupta, A. C., & Wiita, P. J. 2023, ApJ, 943, 53
Lachowicz, P., Gupta, A. C., Gaur, H., & Wiita, P. J. 2009, A&A, 506, L17
Li, Y., Hu, S., Wiita, P. J., & Gupta, A. C. 2018, MNRAS, 478, 172
Liodakis, I., Marchili, N., Angelakis, E., et al. 2017, MNRAS, 466, 4625
Lightkurve Collaboration, Cardoso, J. V. d. M., Hedges, C., et al., 2018 Lightkurve: Kepler and TESS time series analysis in Python, Astrophysics Source Code Library, ascl:1812.013
Marscher, A. P. 2014, ApJ, 780, 87
Miller, H. R., Carini, M. T., & Goodrich, B. D. 1989, Natur, 337, 627

Montagni, F., Maselli, A., Massaro, E., et al. 2006, A&A, 451, 435
Moreno, J., Vogeley, M. S., Richards, G. T., & Yu, W. 2019, PASP, 131, 063001
Pandey, A., Gupta, A. C., Damljanovic, G., et al. 2020, MNRAS, 496, 1430
Pininti, V. R., Bhatta, G., Paul, S., et al. 2023, MNRAS, 518, 1459
Pollack, M., Pauls, D., & Wiita, P. J. 2016, ApJ, 820, 12
Poon, H., Fan, J. H., & Fu, J. N. 2009, ApJS, 185, 511
Qian, B., Tao, J., & Fan, J. 2002, AJ, 123, 678
Raiteri, C. M., Villata, M., Carosati, D., et al. 2021, MNRAS, 501, 1100
Ryan, J. L., Siemiginowska, A., Sobolewska, M. A., & Grindlay, J. 2019, ApJ, 885, 12
Sagar, R., Gopal-Krishna, Mohan, V., et al. 1999, A&AS, 134, 453
Sagar, R., Stalin, C. S., Gopal-Krishna, & Wiita, P. J. 2004, MNRAS, 348, 176
Sillanpaa, A., Haarala, S., Valtonen, M. J., Sundelius, B., & Byrd, G. G. 1988, ApJ, 325, 628
Sillanpaa, A., Takalo, L. O., Pursimo, T., et al. 1996a, A&A, 305, L17
Sillanpaa, A., Takalo, L. O., Pursimo, T., et al. 1996b, A&A, 315, L13

Sitko, M. L., & Junkkarinen, V. T. 1985, PASP, 97, 1158
Smith, P. S., Balonek, T. J., Heckert, P. A., Elston, R., & Schmidt, G. D. 1985, AJ, 90, 1184
Tarnopolski, M., Żywucka, N., Marchenko, V., & Pascual-Granado, J. 2020, ApJS, 250, 1
Valtonen, M. J., Dey, L., Gopakumar, A., et al. 2021, Galax, 10, 1
Valtonen, M. J., Zola, S., Gopakumar, A., et al. 2023, MNRAS, 521, 6143
Vaughan, S. 2005, A&A, 431, 391
Vaughan, S., Edelson, R., Warwick, R. S., & Uttley, P. 2003, MNRAS, 345, 1271
Virtanen, P., Gommers, R., Oliphant, T. E., et al. 2020, NatMe, 17, 261
Wagner, S. J., & Witzel, A. 1995, ARA&A, 33, 163
Wagner, S. J., Witzel, A., Krichbaum, T. P., et al. 1993, A&A, 271, 344
Wehrle, A. E., Carini, M., & Wiita, P. J. 2019, ApJ, 877, 151
Wehrle, A. E., Carini, M., Wiita, P. J., et al. 2023, ApJ, 951, 58
Yu, W., & Richards, G. T., 2022 EzTao: Easier CARMA Modeling, Astrophysics Source Code Library, ascl:2201.001